Variability of vertical structure of precipitation with sea surface temperature over the Arabian Sea and the Bay of Bengal as inferred by TRMM PR measurements

Kadiri Saikranthi[1], Basivi Radhakrishna[2], Thota Narayana Rao[2] and Sreedharan Krishnakumari Satheesh[3]

[1] *Department of Earth and Climate Science, Indian Institute of Science Education and Research (IISER), Tirupati, India.*

[2] *National Atmospheric Research Laboratory, Department of Space, Govt. of India, Gadanki - 517112, India.*

[3] *Divecha Centre for Climate Change, Centre for Atmospheric and Oceanic Sciences, Indian Institute of Science, Bangalore - 560012, India.*

Address of the corresponding author

Dr. K. Saikranthi,
Department of Earth and Climate Science,
Indian Institute of Science Education and Research (IISER),
Tirupati,
Andhra Pradesh, India.
Email: ksaikranthi@gmail.com

Abstract

Tropical rainfall measuring mission precipitation radar measurements are used to examine the variation of vertical structure of precipitation with sea surface temperature (SST) over the Arabian Sea (AS) and Bay of Bengal (BOB). The variation of reflectivity and precipitation echo top with SST is remarkable over the AS but small over the BOB. The reflectivity increases with SST (from 26°C to 31°C) by ~1 dBZ and 4 dBZ above and below 6 km, respectively, over the AS while, its variation is < 0.5 dBZ over the BOB. The transition from shallow storms at lower SSTs (≤ 27°C) to deeper storms at higher SSTs is strongly associated with the decrease in stability and mid-tropospheric wind shear over the AS. Contrary, the storms are deeper at all SSTs over the BOB due to weaker stability and mid-tropospheric wind shear. At lower SSTs, the observed high aerosol optical depth (AOD) and low total column water vapor (TCWV) over AS results in small cloud effective radius (CER) and weaker reflectivity. As SST increases, AOD decreases and TCWV increases leading to large CER and high reflectivity. The changes in these parameters with SST are marginal over the BOB and hence the CER and reflectivity. The predominance of collision-coalescence process below the bright band is responsible for the observed negative slopes in the reflectivity over both the seas. The observed variations in reflectivity are originated at the cloud formation stage over both the seas and these variations are magnified during the descent of hydrometeors to ground.

1. Introduction

Indian summer monsoon (ISM - June through September) is one of the most complex weather phenomena, involving coupling between the atmosphere, land and ocean. At the boundary of the ocean and atmosphere air-sea interactions play a key role for the coupled Earth system (Wu and Kirtman 2005; Feng et al. 2018). The sea surface temperature (SST) – precipitation relations are the important measures for the air-sea interactions on different temporal scales (Woolnough et al., 2000; Rajendran et al. 2012). Recent studies (Wang et al. 2005; Rajeevan et al. 2012; Chaudhari et al. 2013; 2016; Weller et al. 2016; Feng et al. 2018) have shown that the simulation of ISM can be improved with the exact representation of SST - precipitation relationship. SST modulates the meteorological factors that influence the formation and evolution of different kinds of precipitating systems over tropical oceans (Gadgil et al. 1984; Schumacher and Houze, 2003; Takayabu et al. 2010; Oueslati and Bellon 2015).

The studies dealing with SST and cloud/precipitation population considered whole Indian Ocean as a single entity (Gadgil et al. 1984; Woolnough et al., 2000; Rajendran et al. 2012; Sabin et al. 2012; Meenu et al. 2012; Nair and Rajeev 2014; Roxy 2014). But in reality the Bay of Bengal (BOB) and the Arabian Sea (AS) of Indian Ocean possess distinctly different features (Kumar et al. 2014; Shige et al. 2017; Rajendran et al. 2018; Saikranthi et al. 2019). The monsoon experiment (MONEX) and Bay of Bengal monsoon experiment (BOBMEX) have shown how these two seas are different with respect to each other, in terms of SST, back ground atmosphere and the occurrence of precipitating systems (Krishnamurti 1985; Houze and Churchill 1987; Gadgil 2000; Bhat et al. 2001). The SST in the AS cools between 10 °N and 20 °N during the monsoon season whereas warming is seen in other global Oceans between the same latitudes (Krishnamurthi 1981). SST variability is large over the AS than the BOB at seasonal and intraseasonal scales (Sengupta et al. 2001; Roxy et al. 2013). The monsoonal winds (in particular the low-level jet) are stronger over the AS than BOB (Findlater 1969).

Also, lower-tropospheric thermal inversions are more frequent and stronger over the AS than BOB (Narayanan and Rao 1981; Sathiyamoorthy et al. 2013). Thus, the atmospheric and sea surface conditions and in turn the occurrence of different kinds of precipitating systems are quite different over the BOB and the AS during the ISM period. For instance, long-term measurements of tropical rainfall measuring mission (TRMM) precipitation radar (PR) have shown that shallow systems are more prevalent over the AS, while deeper systems occur frequently over the BOB (Liu et al. 2007; Romatschke et al. 2010; Saikranthi et al. 2014, 2018; Houze et al. 2015).

The aforementioned studies mainly focused on the morphology of vertical structure of precipitation, but, none of them studied the variation of vertical structure of precipitation (in terms of occurrence and intensity) with SST and the differences in the vertical structure over AS and BOB. On the other hand, information on the vertical structure of precipitation is essential for improving the accuracy of rainfall estimation (Fu and Liu 2001; Sunilkumar et al. 2015), understanding the dynamical and microphysical processes of hydrometeor growth/decay mechanisms (Houze 2004; Greets and Dejene 2005; Saikranthi et al. 2014; Rao et al. 2016) and for improving the latent heating retrievals (Tao et al. 2006). SST being the main driving force to trigger precipitating systems through air-sea interactions (Sabin et al. 2012; Nuijens et al. 2017), can alter the vertical structure of precipitation (Oueslati and Bellon 2015). Therefore, the present study aims to understand the variation of vertical structure of precipitation (in terms of precipitation top height and intensity) with SST over the AS and BOB. Besides the SST, vertical structure can be modified by aerosols (or CCN, mostly at the cloud formation stage) and thermodynamics of the ambient atmosphere. For instance, recent studies have shown the impact of surface PM_{10} aerosols in altering the vertical structure of precipitation (Guo et al., 2018). All these parameters, therefore, are considered in the present study to explain the differences in the vertical structure.

2. Data

The present study utilizes 16 years (1998-2013) of TRMM-PR's 2A25 (version 7) dataset, comprising of vertical profiles of attenuation corrected reflectivity (Iguchi et al. 2009), during the ISM. The range resolution of TRMM-PR reflectivity profiles is 250 m with a horizontal footprint size of ~4.3 and 5 km before and after the boosting of its orbit from 350 km to 403 km, respectively. It scans ±17° from nadir with a beam width of 0.71° covering a swath of 215 km (245 km after the boost). The uniqueness of TRMM-PR data is its ability in pigeonholing the precipitating systems into convective, stratiform and shallow rain. This classification is based on two methods namely the horizontal method (H - method) and the vertical method (V - method) (Awaka et al. 2009). The original TRMM-PR 2A25 vertical profiles of attenuation corrected reflectivity are gridded to a three dimensional Cartesian coordinate system with a spatial resolution of 0.05° × 0.05°. The detailed methodology of interpolating the TRMM-PR reflectivity data into the 3D Cartesian grid is discussed in Houze et al. (2007). This dataset is available at the University of Washington website (http://trmm.atmos.washington.edu/).

To understand the observed variations in the vertical structure of precipitation in the light of microphysics of clouds, Moderate Resolution Imaging Spectroradiometer (MODIS) AQUA satellite level 3 data (MYD08) are considered. In particular, the daily atmospheric products of aerosol optical depth (AOD) (Hubanks et al. 2008) and cloud effective radius (CER) liquid (Platnick et al. 2017) during the period 2003 and 2013 have been used. MODIS AOD dataset is a collection of aerosol optical properties at 550 nm wavelength, as well as particle size information. Level 2 MODIS AOD is derived from radiances using either one of the three different algorithms, i.e., over ocean Remer et al. (2005) algorithm, over land the Dark-Target (Levy et al. 2007) algorithm and for brighter land surfaces the Deep-Blue (Hsu et al. 2004) algorithm. CER is nothing but the weighted mean of the size distribution of cloud

drops i.e., the ratio of third moment to second moment of the drop size distribution. In the level 3 MODIS daily dataset, aerosol and cloud products of level 2 data pixels with valid retrievals within a calendar day are first aggregated and gridded to a daily average with a spatial resolution of 1° × 1°. For CER grid box values, CER values are weighted by the respective ice/liquid water cloud pixel counts for the spatiotemporal aggregation and averaging processes.

The background atmospheric structure (winds and total column water vapor) and SST information are taken from the European Centre for Medium Range Weather Forecasting (ECMWF) Interim Reanalysis (ERA) (Dee et al. 2011). ERA-Interim runs 4DVAR assimilation twice daily (00 and 12 UTC) to determine the most likely state of the atmosphere at a given time (analysis). The consistency across variables in space and time (during 12-hour intervals) is thus ensured by the atmospheric model and its error characteristics as specified in the assimilation. ERA-Interim is produced at T255 spectral resolution (about 0.75°, ~ 83 km) with a temporal resolution of 6h for upper air fields and 3h for surface fields. The original 0.75° × 0.75° spatial resolution gridded dataset is rescaled to a resolution of 0.125° × 0.125°. The temporal resolution of the dataset used in the present study is 6h (00, 06, 12 and 18 UTC). The equivalent potential temperature (θ_e) is estimated from the ERA-Interim datasets using the following formula (Wallace and Hobbs 2006):

$$\theta_e = \theta exp\left(\frac{L_V w_s}{C_p T}\right) \quad (1)$$

where θ is the potential temperature, L_v is the latent heat of vaporization, w_s is the saturation mixing ratio, C_p is the specific heat at constant pressure and T is the absolute temperature.

The variation of vertical structure of precipitation with SST are studied by considering the dataset between 63 °E – 72 °E and 8 °N – 20 °N over the AS and 83 °E – 92 °E and 8 °N – 21 °N over the BOB. These regions of interest along with the ISM seasonal mean SST over the two seas are depicted in Fig. 1. These regions are selected in such a way that the costal influence

on SST is eluded from the analysis. As the rainfall is scanty over the western AS (west of 63°E latitude) during the ISM (Saikranthi et al. 2018), this region is also not considered in the present analysis. The seasonal mean SST is higher over the BOB than in the AS by more than 1 °C during the ISM season, in agreement with Shenoi et al. (2002). The nearest space and time matched SST data from ERA-Interim are assigned to the TRMM-PR and MODIS observations for further analysis.

3. Variation of vertical structure of precipitation with SST

The occurrence (in terms of %) of conditional precipitation echoes ($Z \geq 17$ dBZ) at different altitudes as a function of SST over the AS and the BOB is shown in Fig. 2. The variation of precipitation echo occurrence frequency with SST is quite different over both the seas. The top of the precipitation echoes extends to higher altitudes with increasing SST over the AS, while such variation is not quite evident over the BOB. Precipitation echoes are confined to < 8 km at lower SST (< 28 °C) over the AS, but exhibits a gradual rise in height with increase in SST. Large population density of precipitation echoes at lower altitudes is mainly due to the abundant occurrence of shallow storms over the AS (Saikranthi et al. 2014, 2019; Rao et al. 2016). Interestingly, the occurrence of precipitation echoes is seen at higher altitudes even at lower SSTs over the BOB, indicating the presence of deeper storms. Such systems exist at all SST's over the BOB.

To examine the variation of reflectivity profiles with SST, median profiles of reflectivity in each SST bin are computed over the AS and the BOB separately for deep and shallow systems and are depicted in Figs. 3 & 4, respectively. The space- and time-matched conditional reflectivity profiles are grouped into 1°C SST bins and then the median is estimated at each height, only if the number of conditional reflectivity pixels (Figs. 3c; 3f; 4c & 4f) is greater than 500. The median reflectivity profiles corresponding to the deep systems are distinctly different over the AS and the BOB (Figs. 3a & 3d), even at the same SST. Over the

AS, reflectivity of deep systems at different SSTs shows small variations (≤ 1 dBZ) above the melting region (> 5 km), but varies significantly (~ 4.5 dBZ) below the melting level (< 5 km). These variations in reflectivity profiles with SST are negligible (< 0.5 dBZ) over the BOB both above and below the melting region. The reflectivity increases from ~ 26.5 dBZ to ~ 31 dBZ, with increase in SST from 26 °C to 30 °C over the AS, but it is almost the same (~ 30dBZ) at all SST's over the BOB below the melting layer. The standard deviation of reflectivity, representing the variability in reflectivity within the SST bin, is similar at all SSTs over both the seas except for the 26 °C SST over AS. At this SST, the standard deviation is lesser by ~ 1 dBZ than that of other SSTs.

The median reflectivity profiles of shallow storms depicted in Figs. 4a & 4d also show a gradual increase in reflectivity from 20 dBZ to ~ 22 dBZ as SST changes from 26 °C to 31 °C at the precipitation top altitude over the AS and don't show any variation with SST over the BOB. However at 1 km altitude, except at 26 °C SST over the AS, the reflectivity variation with SST is not substantial over both the seas. The standard deviation of reflectivity profiles show ~ 1 dBZ variation with SST (from 26 °C to 31°C) at all altitudes over the AS and don't show any variation over the BOB. The standard deviation of reflectivity for shallow storms varies from 3 to 4 dBZ at the precipitation top altitude and 4.5 to 5.3 dBZ at 1 km altitude over the AS while it shows ~ 4 dBZ at precipitation top and ~ 5.5 dBZ at 1 km altitude over the BOB.

4. Factors affecting the vertical structure of precipitation and their variability with SST

The formation and evolution of precipitating systems over oceans depend on dynamical, thermodynamical and microphysical factors, like SST, wind shear, vertical wind velocity, stability, CER, etc., and need to be considered for understanding the vertical structure of precipitation (Li and Min 2010; Creamean et al. 2013; Chen et al. 2015; Shige and Kummerow 2016; Guo et al 2018).

212 **4.1. Dynamical and thermodynamical factors:**

213 Takahashi and Dado (2018) have shown that zonal wind variations can also explain
214 some variability of rain. To examine the impact of zonal wind on rainfall over the Arabian Sea
215 and Bay of Bengal, the data are segregated into 3 wind regimes as weak (monsoon westerlies
216 lies between 0 and 6 m s^{-1}), moderate (monsoon westerlies lies between 6 to 12 m s^{-1}) and
217 strong (monsoon westerlies > 12 m s^{-1}) winds. The median vertical profiles of reflectivity are
218 computed for each SST bin corresponding to deep and shallow systems (not shown here). Two
219 important observations are noted from these figures. 1) Vertical profiles of reflectivity show
220 considerable variation (2-5 dBZ) in all wind categories over the Arabian Sea, but such
221 variations are absent over the Bay of Bengal. It implies that the reported differences in
222 reflectivity profiles over the Arabian Sea and Bay of Bengal exist in all wind regimes. 2) The
223 variation in reflectivity with SST increases with weak to strong wind regime over the Arabian
224 Sea, indicating some influence of wind on reflectivity (rainfall) variation.

225 To understand the role of stability/instability, θ_e values computed from (1) using the
226 ERA-Interim datasets during the ISM period over the AS and the BOB are averaged for a
227 season and are depicted in Figs. 5(a) & 5(b), respectively. The surface θ_e (at 1000 hPa) values
228 are larger over the BOB than those over AS for the same SST, indicating that the instability
229 and convective available potential energy (CAPE) could be higher over the BOB. Indeed,
230 higher CAPE is seen over the BOB (Fig. S1, calculated following Emanuel 1994) than AS at
231 all SSTs by a magnitude > 300 J kg^{-1}. The θ_e increases with SST from 358 °K to 368 °K from
232 27 °C to 31 °C and from 350 °K to 363 °K from 26 °C to 31 °C over the BOB and the AS,
233 respectively. The CAPE also increases with rise in SST over both the seas. To know the
234 stability of the atmosphere θ_e gradients are considered. Irrespective of SST, positive gradients
235 in θ_e are observed between 900 and 800 hPa levels over the AS indicating the presence of
236 strong stable layers. The strength of these stable layers decreases with increasing SST. These

237 stable layers are formed mainly due to the flow of continental dry warm air from Arabian Desert
238 and Africa above the maritime air causing temperature inversions below 750 hPa level over the
239 AS during the ISM period (Narayanan and Rao 1981). However over the BOB, such
240 temperature inversions are not seen in the lower troposphere.

241 To understand the effect of wind field on the vertical structure of precipitation, profiles
242 of ISM seasonal mean vertical wind velocity and vertical shear in horizontal wind at various
243 SSTs over the AS and the BOB are shown in Figs. 5(c), 5(d) & 5(e), 5(f) respectively. The
244 updrafts are prevalent at all SSTs throughout the troposphere over the BOB, whereas
245 downdrafts are seen in the mid-troposphere (between 200 and 600 hPa levels) up to 27 °C and
246 updrafts in the entire troposphere at higher SSTs over the AS. Also, the magnitude of the
247 vertical wind velocity varies significantly with SST in the mid-troposphere over the AS. Over
248 the BOB, the magnitude of updrafts increases with altitude in the lower and middle
249 troposphere, but doesn't vary much with SST. In the mid-troposphere, updrafts are stronger by
250 > 0.02 Pa S^{-1} over the BOB than over the AS. The profiles shown in Fig. 5(e) & 5(f) are the
251 mean vertical shear in horizontal wind estimated following Chen et al. (2015) at different levels
252 with reference to 950 hPa level. The wind shear increases with increasing altitude at all the
253 SSTs up to 400 hPa, but the rate of increase is distinctly different between the AS and the BOB
254 at SSTs less than 28 °C and nearly the same at higher SSTs. The wind shear decreases
255 systematically with SST (~ 1.5 m s^{-1} for 1° increase in SST) in the middle troposphere over the
256 AS while the change is minimal over the BOB (~ 2 m s^{-1} for 27 °C and 31 °C).

257 Chen et al. (2015) highlighted the importance of mid-tropospheric wind shear in
258 generating mesoscale local circulations, like low-level cyclonic and upper-level anticyclonic
259 circulations. This feature is apparent over the AS, where down drafts are prevalent in mid-
260 upper troposphere and updrafts in the lower troposphere at lower SSTs. As SST increases, the
261 wind shear decreases and the updraft increases in the mid-troposphere. However, over the BOB

the wind shear is relatively week when compared to the AS and hence the updrafts are seen up to 200 hPa level at all SSTs. The weaker CAPE and stable mid-troposphere coupled with upper- to mid- tropospheric downdrafts at lower SSTs over the AS inhibit the growth of precipitating systems to higher altitudes and in turn precipitate in the form of shallow rain. This result is in accordance with the findings of Shige and Kummerow (2016) that showed the static stability at lower levels inhibits the growth of clouds and promotes the detrainment of clouds over the Asian monsoon region and is considered as an important parameter in determining the precipitation top height. As SST increases large CAPE and updrafts in the middle troposphere collectively support the precipitating systems to grow to higher altitudes, as evidenced in Fig. 2a. On the other hand, large CAPE and updrafts in the middle troposphere prevalent over the BOB at all SSTs are conducive for the precipitating systems to grow to higher altitudes as seen in Fig. 2b.

4.2. Microphysical factors

The observed differences in reflectivity profiles of precipitation with SST could be originated at the cloud formation stage itself or manifested during the evolution stage or due to both. Information on AOD and CER would be ideal to infer microphysical processes at the cloud formation stage. CER values are mainly controlled by the ambient aerosols concentration and the available moisture (Twomey 1977; Albrecht 1989; Tao et al. 2012; and Rosenfeld et al. 2014). For fixed liquid water content, as the concentration of aerosols increases, the number of cloud drops increases and CER decreases (Twomey 1977). To understand the variation of AOD and TCWV and the resultant CER with SST, the mean AOD and TCWV for different SST bins are plotted in Figs. 6a & 6b. The mean and standard error are calculated only when the number of data points is more than 100 in each SST bin. AOD decreases from 0.62 to 0.31 with rise in SST from 26 °C to 31 °C over the AS but only from 0.42 to 0.36 as SST varies from 27 °C to 30 °C and then increases at higher SSTs over the BOB. The variation of TCWV

287 with SST (Fig. 6b) shows a gradual increase with SST over the AS while it decreases initially
288 from 27°C to 28°C, and then increases over the BOB. At a given SST the TCWV is more in
289 the BOB (> 8 mm) than in the AS.

290 The decrease in AOD and an increase in TCWV with SST result in an increase in CER
291 (14.7 μm to 20.8 μm from 26°C to 31°C) over the AS (Fig. 7). On the other hand, CER doesn't
292 show much variation with SST (18.5 μm to 19.5 μm from 27°C to 31°C) over BOB due to
293 smaller variations in AOD and TCWV. This also shows that the cloud droplets are smaller in
294 size at lower SSTs over the AS than BOB, while they are bigger and nearly equal in size at
295 higher SSTs. Since, reflectivity is more sensitive to the particle size ($Z \propto D^6$), the smaller-
296 sized hydrometeors at lower SSTs over the AS yield weaker reflectivity than over the BOB
297 (both for deep and shallow systems). As the SST increases, CER as well as the reflectivity
298 increases over the AS. At higher SSTs, the CER values are approximately equal over both the
299 seas and in turn the observed reflectivities (Figs. 3a & 4a). This suggests that the variations
300 seen in the reflectivity are originated in the cloud formation stage itself.

301 The hydrometeors also evolve during their descent to the ground due to several
302 microphysical processes. These processes can be inferred from the vertical structure of
303 precipitation or vertical profiles of reflectivity. The median reflectivity profiles of deep systems
304 show a gradual increase from ~ 10 km to 6 km and an abrupt enhancement is seen just below
305 6 km over both the seas (Figs. 3a & 3d). The sudden enhancement at the freezing level (radar
306 bright band) is primarily due to the aggregation of hydrometeors and change in dielectric factor
307 from ice to water (Fabry and Zawadzki 1995; Rao et al. 2008; Cao et al. 2013). Below the
308 bright band, raindrops grow by collision-coalescence process and reduce their size by either
309 breakup and/or evaporation processes. The collision-coalescence results in negative slope in
310 the reflectivity profile, whereas breakup and evaporation results in positive slope (Liu and
311 Zipser 2013; Cao et al. 2013; Saikranthi et al. 2014; Rao et al. 2016). The observed negative

312 slope (~ - 0.3 dBZ km^{-1}) in the median reflectivity profiles below the bright band indicates
313 dominance of low-level hydrometeor growth over both the seas. The magnitude of the slope
314 decreases with SST over the AS, while it is nearly equal at all SSTs over the BOB. It indicates
315 the growth rate decreases with SST over the AS and remains the same at all SSTs over the
316 BOB. The median reflectivity profiles of shallow systems also show negative slopes (~ -1 dBZ
317 km^{-1}) at all SSTs representing the predominance of low-level hydrometeor growth by collision-
318 coalescence processes over both the seas.

319 The present analysis shows that the observed reflectivity changes with SST over both
320 the seas originate at the cloud formation stage and magnify further during the descent of
321 hydrometeors to ground.

322 **5. Conclusions**

323 Sixteen years of TRMM-PR 2A25 reflectivity profiles and 11 years of MODIS AOD
324 and CER data are utilized to understand the differences in variation of vertical structure of
325 precipitation with SST over AS and BOB. Precipitation top height increases with SST over the
326 AS indicating that systems grow to higher altitudes with increase in SST while it is almost
327 same at all SSTs representing that the systems are deeper over the BOB. The decrease in
328 stability and mid-tropospheric wind shear with SST over the AS favour the formation of deeper
329 system at higher systems. However the low stability and small wind shear at all SSTs over the
330 BOB help the formation of deeper systems. The variation of reflectivity with SST is found to
331 be remarkable over the AS and marginal over the BOB. The reflectivity increases with rise in
332 SST over the AS and remains the same at all SSTs over the BOB. This change in reflectivity
333 over the AS is more prominent below the freezing level height (~ 4 dBZ) than the above (~ 1
334 dBZ). Over the AS, the abundance of aerosols and less moisture at SSTs < 27°C result in high
335 concentration of smaller cloud droplets. As SST increases the aerosol concentration decreases
336 and moisture increases leading to the formation of bigger cloud droplets. Thus, the reflectivity

increases with rise in SST over the AS. On the other hand, AOD, TCWV and CER do not show substantial variation with SST over the BOB and hence the change in reflectivity is small. Over the BOB, the mid troposphere is wet and hydrometeor's size at the formation stage is nearly the same at all SSTs. The evolution of hydrometeors during their descent is also similar at all SST's. The collision-coalescence process is predominant below the bright band region over both the seas and is responsible for the observed negative slope in the reflectivity profiles.

Acknowledgements

The authors would like to thank Prof. Robert Houze and his team for the interpolated 3D gridded TRMM-PR dataset (http://trmm.atmos.washington.edu), ECMWF (http://data-portal.ecmwf.int/) team for providing the ERA-Interim dataset and MODIS (https://ladsweb.modaps.eosdis.nasa.gov/) science team for providing the AOD and CER dataset. The authors express their gratitude to Prof. J. Srinivasan for his fruitful discussions and valuable suggestions in improving the quality of the manuscript. The corresponding author would like to thank Department of Science & Technology (DST), India for providing the financial support through the reference number DST/INSPIRE/04/2017/001185. We thank the anonymous referees for their critical comments in improving the quality of the manuscript.

References

Albrecht, B.A.: Aerosols, cloud microphysics, and fractional cloudiness, *Science*, 245, 1227–1230, 1989.

Awaka, J., Iguchi, T., and Okamoto, K.: TRMM PR standard algorithm 2A23 and its performance on bright band detection, *J. Meteorol. Soc. Jpn*., 87A, 31–52, 2009.

Bhat, G. S., Gadgil, S., Kumar, P. V. H., Kalsi, S. R., Madhusoodanan, P., Murty, V. S., Rao, C. V. P., Babu, V. R., Rao, L.V., Rao, R. R., Ravichandran, M., Reddy, K.G., Rao, P. S., Sengupta, D., Sikka, D. R., Swain, J., and Vinayachandran, P. N.: BOBMEX: The Bay of Bengal Monsoon Experiment, *Bull. Amer. Meteor. Soc.,* 82, 2217–2244, 2001.

Cao, Q., Hong, Y., Gourley, J. J., Qi, Y., Zhang, J., Wen, Y., and Kirstetter, P. E.: Statistical and physical analysis of the vertical structure of precipitation in the mountainous west region of the United States using 11+ years of space borne observations from TRMM precipitation radar, *J. Appl. Meteorol. Climatol.*, 52, 408-424, 2013.

Chaudhari, H. S., Pokhrel, S., Kulkani, A., Hazra, A., and Saha, S. K.: Clouds-SST relationship and interannual variability modes of Indian summer monsoon in the context of clouds and SSTs: observational and modelling aspects, *Int. J. Climatol.*, doi: 10.1002/ joc.4664, 2016.

Chaudhari, H. S., Pokhrel, S., Mohanty, S., and Saha, S. K.: Seasonal prediction of Indian summer monsoon in NCEP coupled and uncoupled model, *Theor. Appl. Climatol.*, 114, 459–477, doi:10.1007/s00704-013-0854-8, 2013.

Chen, Q., Fan, J., Hagos, S., Gustafson Jr., W. I., and Berg, L. K.: Roles of wind shear at different vertical levels: Cloud system organization and properties, J. Geophys. Res. Atmos., 120, 6551–6574, 2015.

Creamean, J. M., Suski, K. J., Rosenfeld, D., Cazorla, A., DeMott, P. J., Sullivan, R. C., White, A. B., Ralph, F. M., Minnis, P., Comstock, J. M., Tomlinson, J. M., Kimberly A., and

Prather, K. A.: Dust and biological aerosols from the Sahara and Asia influence precipitation in the western U.S., *Science*, 339, 1572–1578, doi:10.1126/science.1227279, 2013.

Dee, D. P., et al.: The ERA-Interim reanalysis: Configuration and performance of the data assimilation system, *Q. J. R. Meteorol. Soc.*, 137, 553–597, 2011.

Emanuel, K. A.: Atmospheric convection. Oxford University Press, Oxford, 1994.

Fabry, F., and Zawadzki, I.: Long-term radar observations of the melting layer of precipitation and their interpretation, *J. Atmos. Sci.,* 52, 838–851, 1995.

Feng, X., Haines, K., Liu, C., de Boisséson, E., and Polo, I., Improved SST-precipitation intraseasonal relationships in the ECMWF coupled climate reanalysis, *Geophys. Res. Lett.*, 45, 3664–3672, 2018.

Findlater, J.: A major low-level air current near the Indian Ocean during the northern summer, *Q. J. R. Meteorol. Soc.*, 95, 362–380, 1969.

Fu, Y., and Liu, G.: The variability of tropical precipitation profiles and its impact on microwave brightness temperatures as inferred from TRMM data, *J. Appl. Meteorol.*, 40, 2130–2143, 2001.

Gadgil, S., Joseph, P. V., and Joshi, N. V.: Ocean atmosphere coupling over monsoonal regions, *Nature*, 312, 141-143, 1984.

Gadgil, S.: Monsoon–ocean coupling. *Current Sci.,* 78, 309–323, 2000.

Geerts, B., and Dejene, T.: Regional and diurnal variability of the vertical structure of precipitation systems in Africa based on space borne radar data, *J. Clim.*, 18, 893–916, 2005.

Guo, J., Liu, H., Li, Z., Rosenfeld, D., Jiang, M., Xu, W., Jiang, J. H., He, J., Chen, D., Min, M., and Zhai, P.: Aerosol-induced changes in the vertical structure of precipitation: a perspective of TRMM precipitation radar, *Atmos. Chem. Phys*., 18, 13329-13343,

https://doi.org/10.5194/acp-18-13329-2018, 2018.

Houze, R. A., and Churchill, D. D.: Mesoscale organization and cloud microphysics in a Bay of Bengal depression, *J. Atmos. Sci.*, 44, 1845–1867, 1987.

Houze, R. A., Rasmussen, K. L., Zuluaga, M. D., and Brodzik, S. R.: The variable nature of convection in the tropics and subtropics: A legacy of 16 years of the Tropical rainfall measuring mission satellite, *Rev. Geophys.*, 53, 994–1021, 2015.

Houze, R. A., Wilton, D. C., and Smull, B. F.: Monsoon convection in the Himalayan region as seen by the TRMM precipitation radar, *Q. J. R. Meteorol. Soc.,* 133, 1389-1411, 2007.

Houze, R. A.: Mesoscale convective systems, *Rev. Geophys.*, 42, RG4003, doi: 10.1029/2004RG000150, 2004.

Hsu, N., Tsay, S., King, M., and Herman, J.: Aerosol properties over bright-reflecting source regions, *Geosci. Remote Sens. IEEE Trans*., 42, 557–569, 2004.

Hubanks, P., King, M., Platnick, S., and Pincus, R.: MODIS atmosphere L3 gridded product algorithm theoretical basis document collection 005 Version 1.1, Tech. Rep. ATBD-MOD-30, NASA, 2008.

Iguchi, T., Kozu, T., Kwiatkowski, J., Meneghini, R., Awaka, J., and Okamoto, K.: Uncertainties in the rain profiling algorithm for the TRMM precipitation radar, *J. Meteor. Soc. Japan*, 87A, 1–30, doi:10.2151/jmsj.87A.1, 2009.

Krishnamurti, T. N.: Summer monsoon experiment – A review. *Mon. Wea. Rev*., 113, 1590-1626, 1985.

Krishnamurti, T.: Cooling of the Arabian Sea and the onset-vortex during 1979. Recent progress in equatorial oceanography: A report of the final meeting of SCOR WORKING GROUP 47 in Venice, Italy, 1-12, 1981. [Available from Nova Univ., Ocean Science Center, Dania, FL 33004].

Kumar, S., Hazra, A., and Goswami, B. N.: Role of interaction between dynamics,

thermodynamics and cloud microphysics on summer monsoon precipitating clouds over the Myanmar coast and the Western Ghats, *Clim. Dyn*., 43, 911–924, doi:10.1007/s00382-013-1909-3, 2014.

Levy, R., Remer, L., Mattoo, S., Vermote, E., and Kaufman, Y.: Second-generation operational algorithm: Retrieval of aerosol properties over land from inversion of moderate resolution imaging spectroradiometer spectral reflectance, *J. Geophys. Res*., 112, D13, doi:10.1029/2006JD007811, 2007.

Li, R., and Min, Q.-L.: Impacts of mineral dust on the vertical structure of precipitation, J. Geophys. Res., 115, D09203, doi:10.1029/2009JD011925, 2010.

Liu, C., Zipser, E., and Nesbitt, S. W.: Global distribution of tropical deep convection: Different perspectives using infrared and radar as the primary data source, *J. Climate*, 20, 489-503, 2007.

Liu. C., and Zipser, E. J.: Why does radar reflectivity tend to increase downward toward the ocean surface, but decrease downward toward the land surface?, *J. Geophys. Res. Atmos.*, 118, 135-148, doi: 10.1029/2012JD018134, 2013.

Meenu, S., Parameswaran, K., and Rajeev, K.: Role of sea surface temperature and wind convergence in regulating convection over the tropical Indian Ocean, *J. Geophys. Res. Atmos.*, 117, D14102, 2012.

Nair, A. K. M., and Rajeev, K.: Multiyear CloudSat and CALIPSO observations of the dependence of cloud vertical distribution on sea surface temperature and tropospheric dynamics, *J. Clim*., 27, 672–683, doi:10.1175/JCLI-D-13-00062.1, 2014.

Narayanan, M. S., and Rao, B. M.: Detection of monsoon inversion by TIROS-N satellite, *Nature*, 294, 546-548, 1981.

Nuijens, L., Emanuel, K., Masunaga, H., and L'Ecuyer, T.: Implications of warm rain in shallow cumulus and congestus clouds for large-scale circulations, *Surv. Geophys*., 38,

1257-1282, 2017.

Oueslati, B., and Bellon, G.: The double ITCZ bias in CMIP5 models: interaction between SST, large-scale circulation and precipitation. *Clim. Dyn.*, 44, 585-607, 2015.

Platnick, S., et al.: The MODIS cloud optical and microphysical products: Collection 6 updates and examples from Terra and Aqua, *IEEE Trans. Geosci. Remote Sens*., 55, 502–525, doi:10.1109/TGRS.2016.2610522, 2017.

Rajeevan, M., Unnikrishnan, C. K., and Preethi, B.: Evaluation of the ENSEMBLES multi-model seasonal forecasts of Indian summer monsoon variability, *Clim. Dyn.*, 38, 2257–2274, 2012.

Rajendran, K., Nanjundiah, R. S., Gadgil, S., and Srinivasan, J.: How good are the simulations of tropical SST–rainfall relationship by IPCC AR4 atmospheric and coupled models?, *J. Earth Sys. Sci.*, 121(3), 595–610, 2012.

Rajendran, K., Gadgil, S. and Surendran, S.: Monsoon season local control on precipitation over warm tropical oceans, *Meteorol. Atmos. Phys*., doi:10.1007/s00703-018-0649-7, 2018.

Rao, T. N., Kirankumar, N. V. P., Radhakrishna, B., Rao, D. N., and Nakamura, K.: Classification of tropical precipitating systems using wind profiler spectral moments. Part I: Algorithm description and validation, *J. Atmos. Oceanic Technol.,* 25, 884–897, 2008.

Rao, T. N., Saikranthi, K., Radhakrisna, B., and Rao, S. V. B.: Differences in the climataological characteristics of precipitation between active and break spells of the Indian summer monsoon, *J. Clim.*, 29, 7797-7814, 2016.

Remer, L., Kaufman, Y., Tanr´e, D., Mattoo, S., Chu, D., Martins, J., Li, R., Ichoku, C., Levy, R., Kleidman, R., Eck, T., Vermote, E., and Holben, B.: The MODIS aerosol algorithm, products, and validation, *J. Atmos. Sci*., 62, 947–973, 2005.

489 Romatschke, U., Medina, S., and Houze, R. A.: Regional, seasonal, and diurnal variations of
490 extreme convection in the South Asian region, *J. Clim.*, 23, 419 –439, 2010.
491 Rosenfeld, D., et al.: Global observations of aerosol-cloud-precipitation-climate interactions,
492 *Rev. Geophys.*, 52, 750-808, doi:10.1002/2013RG000441, 2014.
493 Roxy, M., Tanimoto, Y., Preethi, B., Terray, P., and Krishnan, R.: Intraseasonal SST-
494 precipitation relationship and its spatial variability over the tropical summer monsoon
495 region, *Clim. Dyn.*, 41, 45-61, 2013.
496 Roxy, M.: Sensitivity of precipitation to sea surface temperature over the tropical summer
497 monsoon region—and its quantification, *Clim. Dyn.*, 43, 1159-1169, 2014.
498 Sabin, T., Babu, C., and Joseph, P.: SST–convection relation over tropical oceans, *Int. J.*
499 *Climatol*. 33, 1424–1435, 2012.
500 Saikranthi, K., Radhakrishna, B., Satheesh, S. K., and Rao, T. N.: Spatial variation of
501 different rain systems during El Niño and La Niña periods over India and adjoining
502 ocean, *Clim. Dyn.*, 50, 3671-3685, doi: 10.1007/s00382-017-3833-4, 2018.
503 Saikranthi, K., Rao, T. N., Radhakrishna, B., and Rao, S. V. B.: Morphology of the vertical
504 structure of precipitation over India and adjoining oceans based on long-term
505 measurements of TRMMPR, *J. Geophys. Res. Atmos.*, 119, 8433–8449, doi:
506 10.1002/2014JD021774, 2014.
507 Saikranthi, K., Radhakrishna, B., Rao, T. N., and Satheesh, S. K.: Differences in the association
508 of sea surface temperature - precipitating systems over the Bay of Bengal and the Arabian
509 Sea during southwest monsoon season. *Int. J. Climatol*., doi:10.1002/joc.6074, 2019.
510 Sathiyamoorthy, V., Mahesh, C., Gopalan, K., Prakash, S., Shukla, B. P., Mathur, A.:
511 Characteristics of low clouds over the Arabian Sea, *J. Geophys. Res. Atmos.*, 118, 13489-
512 13503, 2013.

513 Schumacher, C. and Houze, R. A.: Stratiform rain in the tropics as seen by the TRMM
514 precipitation radar, *J. Climate.*, 16, 1739–1756, 2003.
515 Sengupta, D., Goswami, B. N., and Senan, R.: Coherent intraseasonal oscillations of ocean and
516 atmosphere during the Asian summer monsoon, *Geophys. Res. Lett.*, 28, 4127–4130,
517 2001.
518 Shenoi, S. S. C., Shankar, D., and Shetye, S. R.: Differences in heat budgets of the near-surface
519 Arabian Sea and Bay of Bengal: Implications for the summer monsoon, *J. Geophys. Res.*,
520 107(C6), 3052, doi:10.1029/2000JC000679, 2002.
521 Shige, S. and Kummerow, C.D.: Precipitation-Top Heights of Heavy Orographic Rainfall in
522 the Asian Monsoon Region, *J. Atmos. Sci.,* 73, 3009–3024, 2016.
523 Shige, S., Nakano, Y., and Yamamoto, M. K.: Role of orography, diurnal cycle, and
524 intraseasonal oscillation in summer monsoon rainfall over Western Ghats and Myanmar
525 coast, *J. Climate*, 30, 9365–9381, doi:10.1175/JCLI-D-16-0858.1, 2017.
526 Sunilkumar, K., Rao, T. N., Saikranthi, K., and Rao, M. P.: comprehensive evaluation of
527 multisatellite precipitation estimates over India using gridded rainfall data, *J. Geophys.*
528 *Res. Atmos.*, 120, doi:10.1002/2015JD023437, 2015.
529 Takahashi, H. G., and Dado, J. M. B.: Relationship between sea surface temperature and
530 rainfall in the Philippines during the Asian summer monsoon, *J. Meteor. Soc. Japan*,, 96
531 (3), 283−290, doi:10.2151/jmsj.2018-03, 2018.
532 Takayabu, Y. N., Shige, S., Tao, W., and Hirota, N.: Shallow and deep latent heating modes
533 over tropical Oceans observed with TRMM PR spectral latent heating Data, *J. Climate,*
534 23, 2030–2046, 2010.
535 Tao, W.-K., Chen, J.-P., Li, Z., Wang, C., and Zhang, C.: Impact of aerosols on convective
536 clouds and precipitation, *Rev. Geophys.*, 50, RG2001, doi:10.1029/2011RG000369,
537 2012.

538 Tao, W.-K., et al.: Retrieval of latent heating from TRMM measurements, *Bull. Am. Meteorol.*
539 *Soc.*, 87, 1555–1572, 2006.
540 Twomey, S.: The influence of pollution on the short wave albedo of clouds, *J. Atmos. Sci.*, 34,
541 1149–1152, 1977.
542 Wallace, J. M., and Hobbs, P. V.: Atmospheric science: An introductory survey, Second
543 edition, Academic press, pp. 85, 2006.
544 Wang, B., Ding, Q., Fu, X., Kang, I.-S., Jin, K., Shukla, J., and Doblas-Reyes, F.: Fundamental
545 challenge in simulation and prediction of summer monsoon rainfall, *Geophys. Res. Lett*.,
546 32, L15711, doi:10.1029/2005GL022734, 2005.
547 Weller, R. A., Farrar, J. T., Buckley, J., Mathew, S., Venkatesan, R., Lekha, J. S., Chaudhuri,
548 D., Kumar, N. S., and Kumar, B. P.: Air-sea interaction in the Bay of Bengal,
549 *Oceanography*, 29(2), 28–37, 2016.
550 Woolnough, S.J., Slingo, J.M., and Hoskins, B.J.: The relationship between convection and sea
551 surface temperature on intraseasonal timescales, *J. Climate,* 13, 2086–2104, 2000.
552 Wu, R., and Kirtman, B. P.: Roles of Indian and Pacific Ocean air–sea coupling in tropical
553 atmospheric variability, *Clim. Dyn.*, *25*(2–3), 155–170, 2005.
554
555
556
557
558
559
560
561
562

563 **Figure captions**

564 **Figure 1:** Spatial distribution of ISM mean SST (in °C) obtained from ERA-Interim reanalysis
565 data over the AS (63°E-72°E & 8°N-20°N) and the BOB (83°E-92°E & 8°N-21°N).
566 The regions considered in this analysis over these two seas are shown with the boxes.

567 **Figure 2:** (a) and (b) represent the altitudinal distribution of occurrence of conditional
568 reflectivity (≥ 17 dBZ) as a function of SST with respect to precipitation occurrence at
569 that particular SST interval over the AS and the BOB, respectively.

570 **Figure 3:** (a), (d) and (b), (e) represent vertical profiles of median reflectivity correspond to
571 deep systems and their standard deviation (in dBZ) with SST over the AS and the BOB,
572 respectively during the ISM season. (c) and (f) show the number of conditional
573 reflectivity pixels at each altitude used for the estimation of the median and standard
574 deviation.

575 **Figure 4:** Same as Fig. 3 but for shallow precipitating systems.

576 **Figure 5:** (a) and (b), respectively, represent the vertical profiles of mean θ_e (in K) with SST
577 over the AS and the BOB during the ISM season. (c) and (d) and (e) and (f) are same
578 as (a) and (b) but for mean vertical velocity (in Pa s^{-1}) and wind gradient with reference
579 to 950 hPa level (in m s^{-1}).

580 **Figure 6:** (a) Mean and standard error of AOD and (b) TCWV (in mm) with SST over the AS
581 and the BOB during ISM.

582 **Figure 7:** Variation of mean and standard error of CER liquid (in μm) with SST over the AS
583 and the BOB during the ISM season.

584
585
586
587
588

589 **Figures**

590

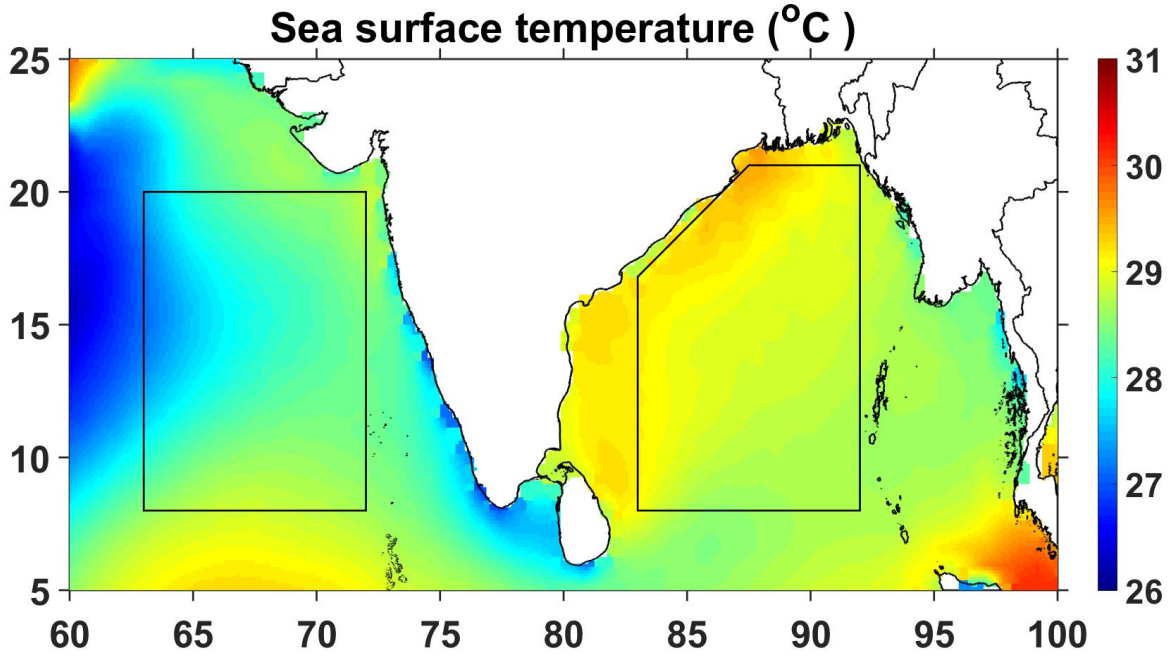

591

592 **Figure 1:** Spatial distribution of ISM mean SST (in °C) obtained from ERA-Interim reanalysis
593 data over the AS (63°E-72°E & 8°N-20°N) and the BOB (83°E-92°E & 8°N-21°N).
594 The regions considered in this analysis over these two seas are shown with the boxes.

595

596

597

598

599

600

601

602

603

604

605

606

607

608

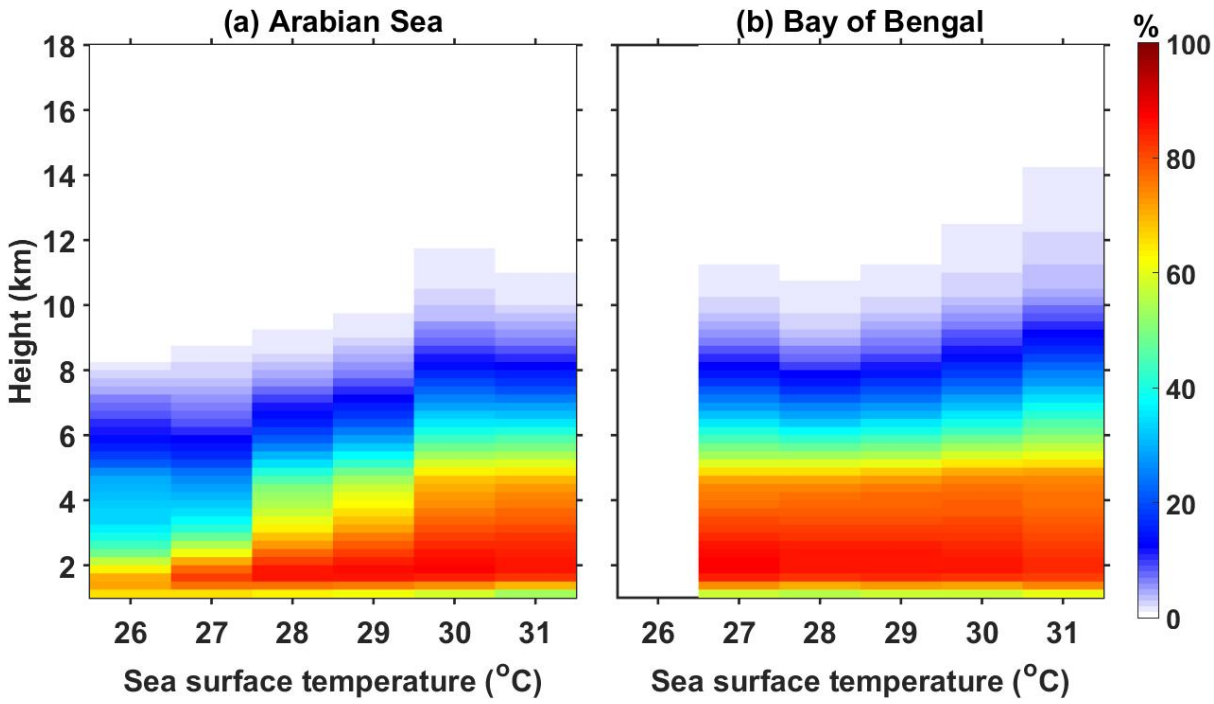

Figure 2: (a) and (b) represent the altitudinal distribution of occurrence of conditional reflectivity (≥ 17 dBZ) as a function of SST with respect to precipitation occurrence at that particular SST interval over the AS and the BOB, respectively.

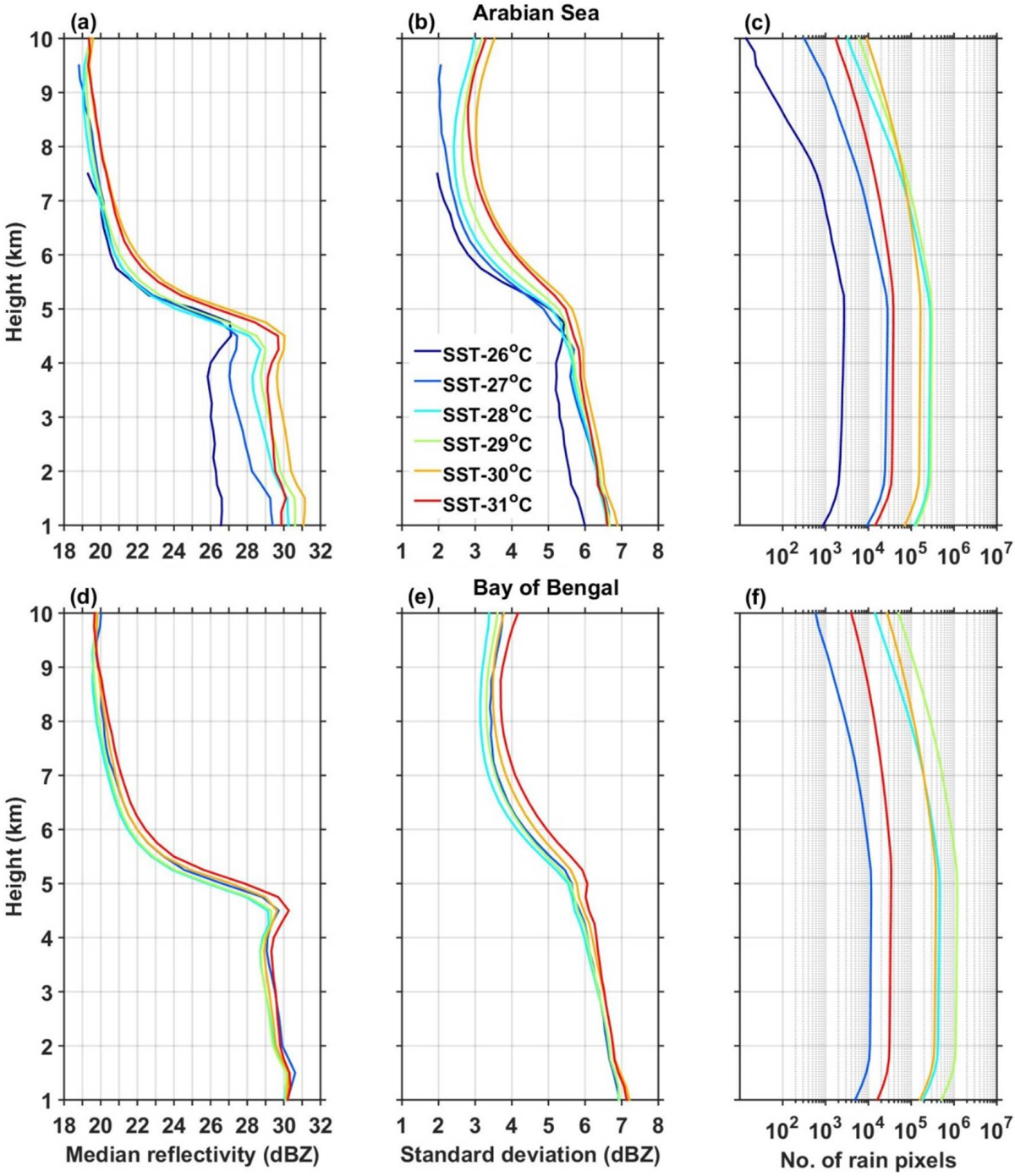

Figure 3: (a), (d) and (b), (e) represent vertical profiles of median reflectivity correspond to deep systems and their standard deviation (in dBZ) with SST over the AS and the BOB, respectively during the ISM season. (c) and (f) show the number of conditional reflectivity pixels at each altitude used for the estimation of the median and standard deviation.

639

640

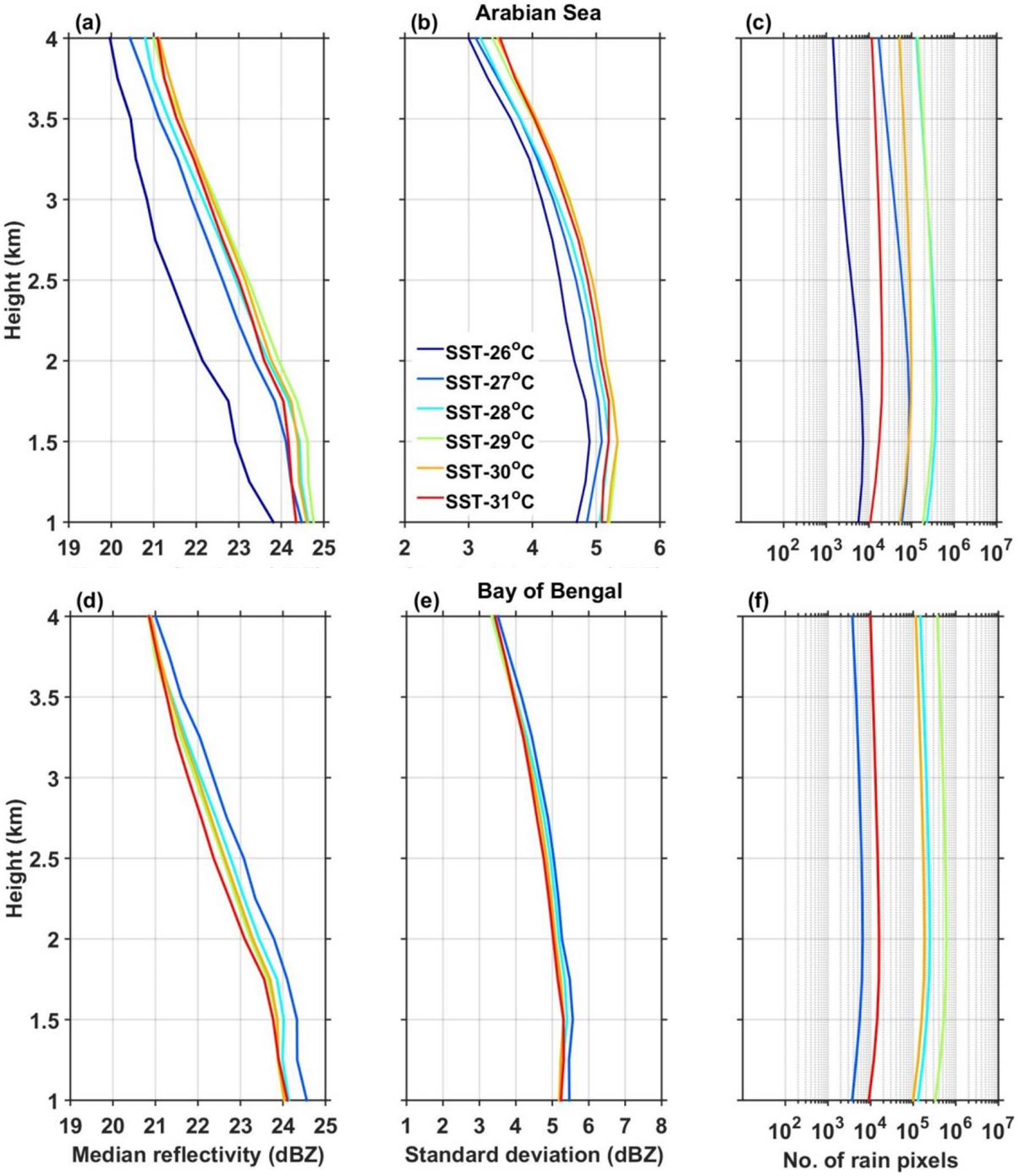

641

642 **Figure 4:** Same as Fig. 3 but for shallow precipitating systems.

643

644

645

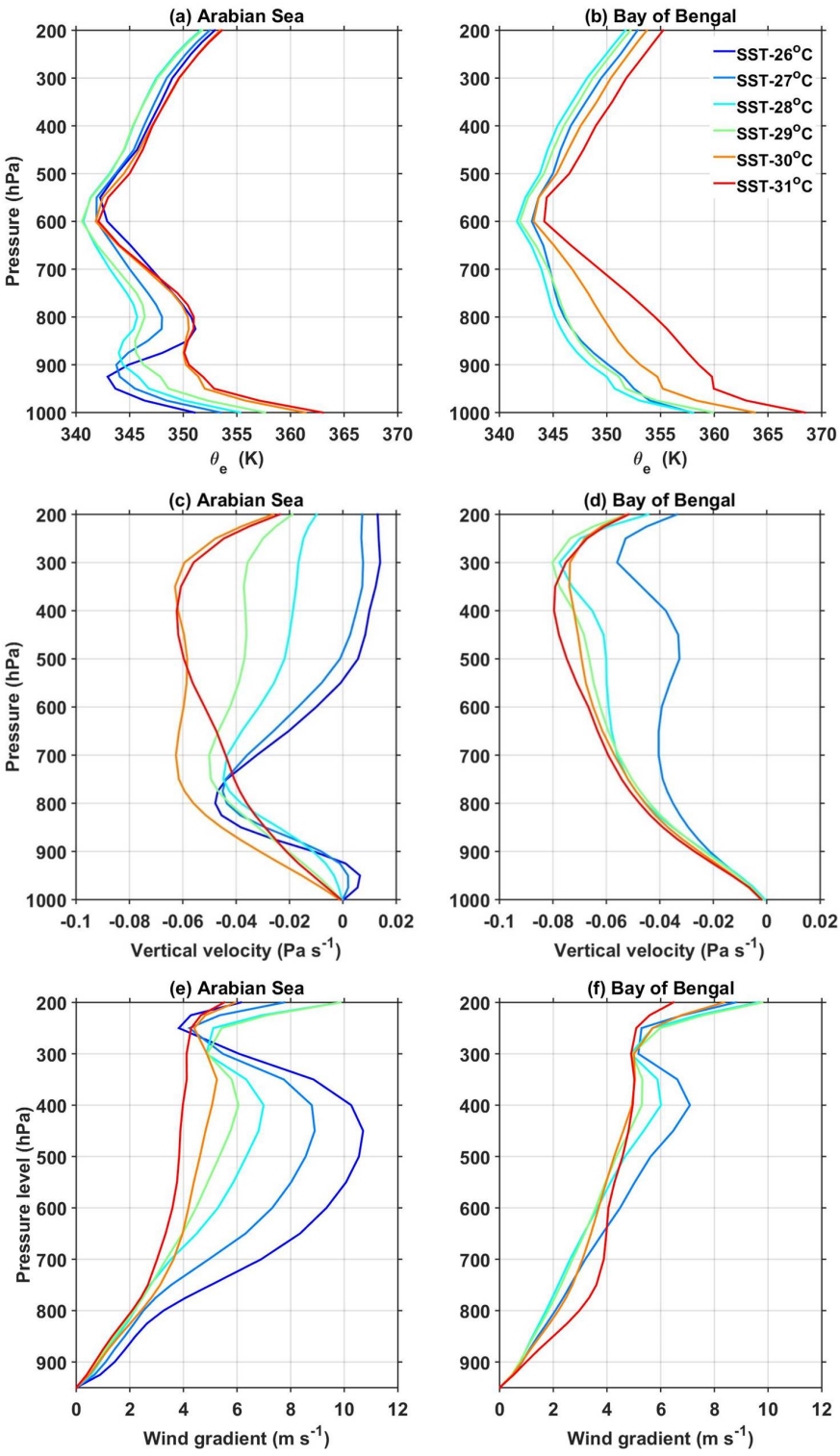

Figure 5: (a) and (b), respectively, represent the vertical profiles of mean θ_e (in K) with SST over the AS and the BOB during the ISM season. (c) and (d) and (e) and (f) are same as (a) and (b) but for mean vertical velocity (in Pa s^{-1}) and wind gradient with reference to 950 hPa level (in m s^{-1}).

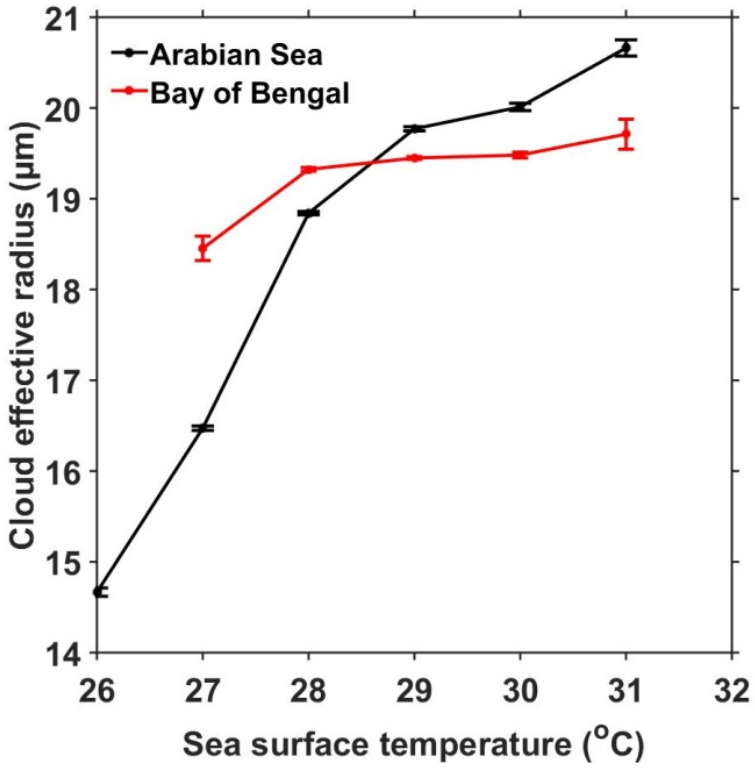

Figure 6: Variation of mean and standard error of CER liquid (in μm) with SST over the AS and the BOB during the ISM season.

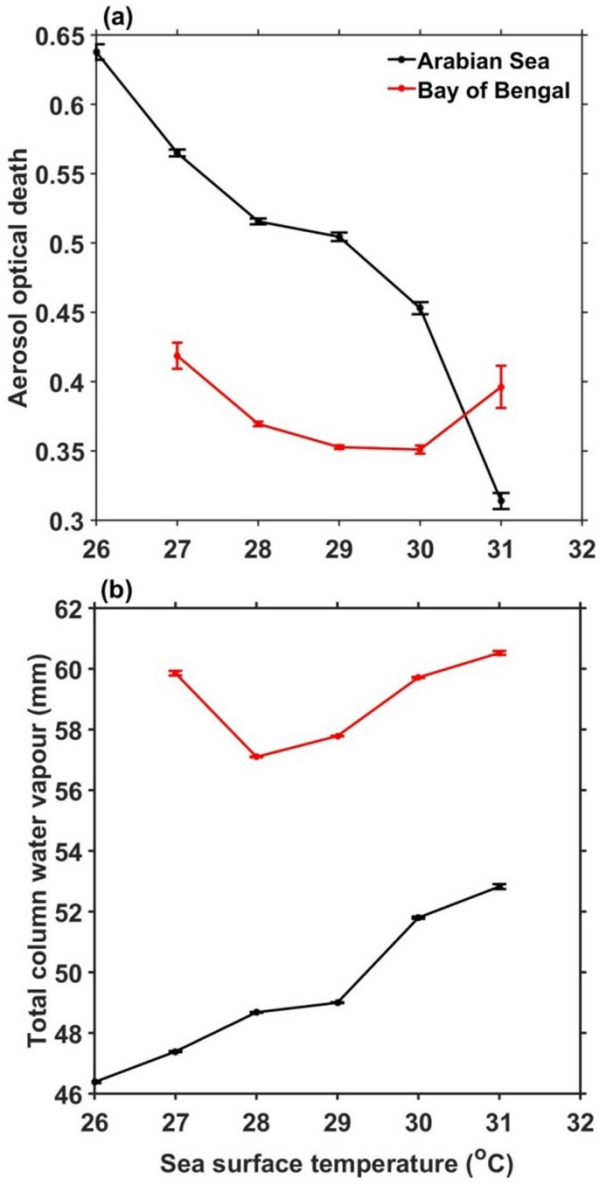

Figure 7: (a) Mean and standard error of AOD and (b) TCWV (in mm) with SST over the AS and the BOB during ISM.

738 **Supplementary material**

739 Satheesh et al. (2006) showed an increase in AOD with increase in latitude over the AS due to
740 the dust advection from Arabia desert regions during ISM season, whereas SST decreases with
741 increase in the latitude. In other words the SST is low and AOD is high in northern AS whereas
742 over the southern AS, SST is high and AOD is low. This contrasting spatial distribution of
743 AOD and SST could cause a negative correlation between AOD and SST as depicted in Fig.
744 6a. To examine whether the observed decrease in AOD with increase in SST over the AS is
745 due to the latitudinal variation of AOD or exists at all latitudes, we have segregated the data
746 into 2° latitude bins and plotted the mean AOD with SST for all bins and is depicted in Fig. S2.
747 In spite of the magnitude, AOD variation with SST is nearly similar at all latitudes of the AS,
748 i.e., the higher AOD is observed at lower SSTs and vice versa (Fig. S2a). On the other hand
749 the latitudinal variation of AOD with SST over the BOB shown in Fig. S2b also show a
750 decrease in AOD with SST till 30 °C but the magnitude of variation is trivial relative to the
751 AS. Also, as depicted in Fig. 6a AOD increases above 30 °C with SST over the BOB. This
752 indicates that though there is a difference in magnitude of variation, AOD varies with SST over
753 both the seas at all latitudes. This analysis is repeated using the multi-angle imaging
754 spectroradiometer (MISR) dataset (which is not shown here) for small, medium large aerosol
755 particles. Interestingly all three types also show a decrease in AOD with rise in SST over both
756 the seas.

757

758 Satheesh, S. K., Moorthy, K. K., Kaufman, Y. J., and Takemura, T.: Aerosol Optical depth,
759 physical properties and radiative forcing over the Arabian Sea, *Meteorol. Atmos.*
760 *Phys.*, 91, 45–62, doi:10.1007/s00703-004-0097-4, 2006.

761

762

763

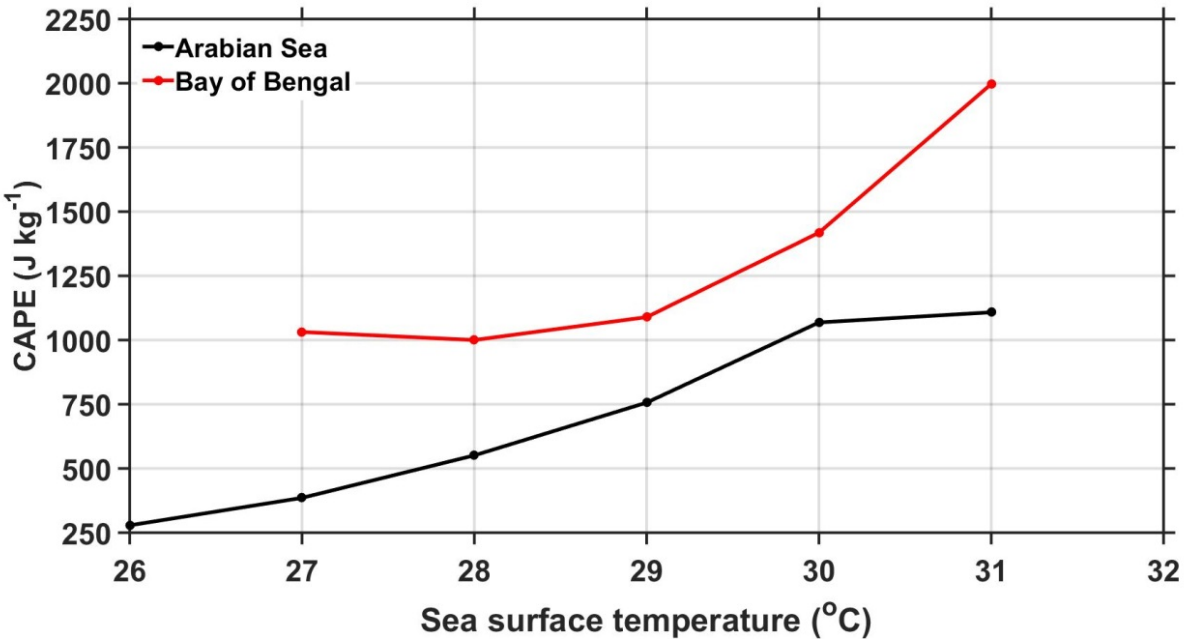

Figure S1: Variation of mean CAPE (in J kg^{-1}) with SST over the AS and the BOB during the ISM season.

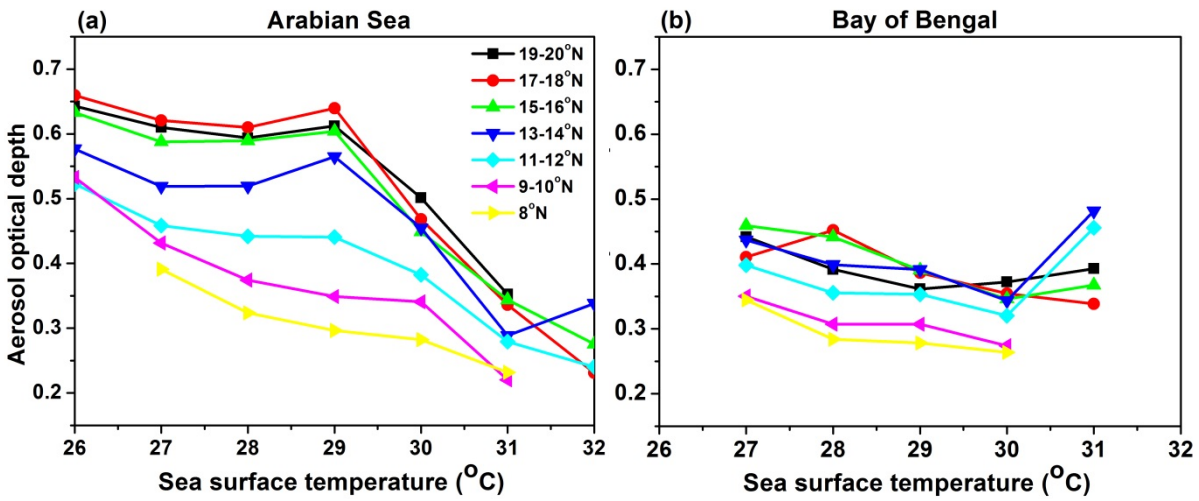

Figure S2: (a) and (b), respectively, represent latitudinal variation (for every 2° latitude interval) of mean AOD over the AS (between 63°E and 72°E) and the BOB (between 83°E and 92°E).